Monte Carlo Simulation of Transport in Technologically Significant Semiconductors of the Diamond and Zinc-Blende Structures—Part I: Homogeneous Transport

Massimo V. Fischetti

Abstract—**Monte Carlo simulations of electron transport in seven semiconductors of the diamond and zinc-blende structure (Ge, Si, GaAs, InP, AlAs, InAs, GaP) and some of their alloys ($Al_xGa_{1-x}As$, $In_xGa_{1-x}As$, $Ga_xIn_{1-x}P$), and hole transport in Si have been performed at two lattice temperatures (77 and 300 K). The model employs band structures obtained from local empirical pseudopotential calculations and particle-lattice scattering rates computed from the Fermi Golden Rule accounting for band-structure effects. Intervalley deformation potentials significantly lower than those previously reported in the Monte Carlo literature are needed to reproduce available experimental data. This is attributed to the more complicated band structures we have adopted, particularly around the *L*- and *X*-symmetry points in most materials. Despite the satisfactory agreement obtained between Monte Carlo results and some experiments, the inconsistency or lack of experimental information regarding the band structure (AlAs, GaP, InP), velocity-field characteristics (GaP, InAs, $Al_xGa_{1-x}As$, $Ga_xIn_{1-x}P$), and impact ionization coefficients (InAs) of many materials indicate that a significant uncertainty still remains in our ability to describe the charge transport in many of these technologically significant materials.**

I. Introduction

THE present paper is a prerequisite to a companion one [1], in which Monte Carlo (MC) simulations will be used to investigate the behavior of very small metal–oxide–semiconductor field-effect transistors (MOSFET's) built on a variety of technologically important group IV materials and III–V compounds. Since the results of this investigation may be somewhat surprising, it is necessary to spell out as accurately as possible the assumptions, approximations, and parametrizations employed in the modeling. In order to help the readability of the presentation, we have divided it in two parts. In this paper we shall present results of steady-state and homogeneous MC simulations of electron transport in seven materials (Ge, Si, GaAs, InP, AlAs, InAs, and GaP), 3 ternary alloys ($Al_xGa_{1-x}As$, $In_xGa_{1-x}As$, and $Ga_xIn_{1-x}P$), and hole transport in Si, in every case compared to available experimental data. In the companion paper [1] we shall present our results related to the simulation of small (channel length $\lesssim 0.25\ \mu m$) MOSFET's.

In this first paper, we shall start by presenting briefly our MC strategy. We shall then discuss the band structure of the materials and move, finally, to MC results: drift velocities, average energies, impact-ionization coefficients, relaxation times, and diffusivities versus electric field. Unfortunately, most of the presentation will have the flavor of a "cold" list of tables and figures, much of the discussion being limited to specific issues about the lack or inconsistency of experimental data. However, we feel that such an uninspiring list is made necessary by the variety of (and confusion surrounding) parameters used by various authors to simulate transport in semiconductors. Therefore, a detailed presentation of our basic material modeling is needed before we can move to device modeling. In addition, many of the physical parameters we have chosen (mainly: band structures and deformation potentials) are different from those commonly employed in the Monte Carlo literature, particularly for III–V compounds. Therefore, the present paper may have some merit on its own, clarifying, hopefully, some features of charge transport in these materials.

Manuscript received May 8, 1990; revised October 9, 1990. The review of this paper was arranged by Associate Editor M. D. Feuer.

The author is with the IBM Research Division, Thomas J. Watson Research Center, P.O. Box 218, Yorktown Heights, NY 10598.

IEEE Log Number 9041218.

II. Monte Carlo Technique

The Monte Carlo technique we have employed has been described in detail before [2]. Here we shall only summarize its features.

A. Band Structure

The band structure of the semiconductor is obtained following the local empirical pseudopotential approach of Cohen and Bergstresser [3], to permit a better description of hot-carrier transport than it is usually provided by "low-energy" MC simulations employing parabolic or first-order nonparabolic bands (see [5]–[9] for covalent materials, [10]–[14] for III–V compounds, [15] for a review of the MC technique). This approach has been pioneered by Hess and co-workers [16]–[18] for Si and GaAs and extended to other III–V compounds by Brennan and co-workers [19], [20]. Their results and our previous simulations [2] have stressed the importance of a better description of the band structure to analyze high-field transport, as it occurs in submicrometer devices.

For the numerical implementation, we have tabulated the energies and energy gradients (i.e., the group velocities) for the first five conduction bands in a mesh of 916 points in the irreducible wedge of the first Brillouin zone (BZ), corresponding to cubic mesh elements of size 0.05 in units of $2\pi/a$, a being the lattice constant. A quadratic (for energies) or linear (for gradients) interpolation is used during the integration of the equa-

0018-9383/91/0300-0634$01.00

tions of motion of the carriers during the free-flights between collisions

$$\frac{d\boldsymbol{r}}{dt} = \frac{1}{\hbar}\nabla_{\boldsymbol{k}}[E_\nu(\boldsymbol{k})] \tag{1a}$$

$$\frac{d\boldsymbol{k}}{dt} = -\frac{e\boldsymbol{F}(\boldsymbol{r})}{\hbar} \tag{1b}$$

where $\boldsymbol{r}$ is the particle coordinate in real space, $\boldsymbol{k}$ is the wave vector, $\boldsymbol{F}(\boldsymbol{r})$ is the electric field at position $\boldsymbol{r}$, $\hbar$ is the reduced Planck constant, and $E_\nu(\boldsymbol{k})$ is the energy of a particle of wave vector $\boldsymbol{k}$ in the band of index ν. Notice that, as discussed elsewhere [2], the small value of the effective mass in the Γ-valley of many materials prevents a sufficiently accurate interpolation of the band structure around the symmetry point Γ, when a realistically small number of $\boldsymbol{k}$ points is used to discretize the BZ. Therefore, we have chosen to treat "analytically" the band structure in the proximity of Γ, by using a nonparabolic Γ valley up to energies about 0.3 eV above the Γ minimum in most III–V semiconductors. Care was taken to ensure that all intervalley processes were treated using the empirical-pseudopotential band structure, for reasons discussed below.

As far as the valence bands are concerned, the structure around the Γ point complicates once again both the physical and the numerical aspects of the simulation. To date, we have limited our analysis to the valence bands of Si, since the low spin-orbit coupling of this material [21], [22] allows a satisfactory treatment of the valence bands with the local pseudopotentials of [3] which ignores spin-orbit corrections. An "analytical" approach, similar to the one used for the conduction band around Γ, was unsuitable, because of the warping and nonparabolicity of the bands. Thus in this case, we had to employ a much finer discretization of $\boldsymbol{k}$ space around the Γ point in order to resolve the hole dispersion with sufficient accuracy. A nested interpolation similar to the one described in [2] was used, but with a further level of "nesting," dividing the central region $k_x, k_y, k_z \leq 0.2(2\pi/a)$ into even smaller cubes with sides of length $0.0125\ (2\pi/a)$.

Finally, the electron dispersion for ternary alloys of the type $A_xB_{1-x}C$ has been obtained from the linear interpolation

$$E_{\text{alloy}}(\boldsymbol{k}, x) = xE_{AC}(\boldsymbol{k}) + (1-x)E_{BC}(\boldsymbol{k}) - E_{0,x} \tag{2}$$

where $E_{0,x}$ is the bottom of the conduction band, $E_{AC}(\boldsymbol{k})$ and $E_{BC}(\boldsymbol{k})$ are the energies in the binary semiconductors AC and BC, measured from the respective conduction-band minima. Bowing effects, as significant as they might be, cannot be accounted for in any easy way when a $\boldsymbol{k}$-dependent bowing is observed experimentally. Thus a fixed bowing was used only to account for the variation of the bandgap with mole fraction x. It is difficult to estimate the errors caused by this approximation, as the experimental information about the bowing parameters at the various symmetry points Γ, L, and X is somewhat incomplete for III–V ternary compounds. We shall mention below the case of $In_{0.53}Ga_{0.47}As$, for which our interpolation and the experimental observations are in disagreement.

B. Carrier–Phonon Interaction

The electron–phonon scattering rates have been calculated accounting for the "exact" density of final states, but employing a phenomenological approach for the matrix elements. This has been described in [2]. Here we shall briefly spell out the relevant formulas for completeness. The nonpolar scattering rate, $1/\tau_{\eta,\nu}(\boldsymbol{k})$, between an electron of wave vector $\boldsymbol{k}$ in the νth band and a phonon of type (acoustic or optical, transverse or longitudinal) η has been calculated from the Golden Rule expression

$$\frac{1}{\tau_{\eta,\nu}(\boldsymbol{k})} = \sum_{\nu',\boldsymbol{q}} \frac{\pi}{\rho\omega_{\eta,\boldsymbol{q}}} \Delta_{\eta,\nu'}(\boldsymbol{q})^2 \left|\mathcal{I}(\nu, \nu'; \boldsymbol{k}, \boldsymbol{k}')\right|^2 \cdot \delta(E_\nu - E'_{\nu'} \mp \hbar\omega_{\eta,\boldsymbol{q}}) \left(n_{\eta,\boldsymbol{q}} + \frac{1}{2} \pm \frac{1}{2}\right) \tag{3}$$

while in a polar semiconductor the rate for the polar collisions with longitudinal optical phonons $1/\tau_{LO}(\boldsymbol{k})$ is given by

$$\frac{1}{\tau_{LO}(\boldsymbol{k})} = \frac{2\pi}{\hbar}\sum_{\boldsymbol{q}} \frac{e^2F^2}{q^2} \left|\mathcal{I}(\nu, \mu; \boldsymbol{k}, \boldsymbol{k}')\right|^2 \cdot \delta(E - E' \mp \hbar\omega_{\text{LO}}) \left(n_{\text{LO}} + \frac{1}{2} \pm \frac{1}{2}\right). \tag{4}$$

In these formulas the upper and lower signs correspond to emission and absorption of a phonon, respectively, while ρ is the density of the semiconductor, $\Delta_{\eta,\nu'}(\boldsymbol{q})$ is a coupling constant, $\omega_{\eta,\boldsymbol{q}}$ is the frequency of the phonon of type η and wave vector $\boldsymbol{q}$, $\boldsymbol{k}' = \boldsymbol{k} \mp \boldsymbol{q} + \boldsymbol{G}$ is the final electron wave vector which is mapped into the first BZ by adding a vector $\boldsymbol{G}$ of the reciprocal lattice. Also, $\mathcal{I}$ is the overlap integral, $E_\nu = E_\nu(\boldsymbol{k})$, $E'_{\nu'} = E_{\nu'}(\boldsymbol{k} \mp \boldsymbol{q})$, and $n_{\eta,\boldsymbol{q}}$ is the phonon occupation number at the lattice temperature T. The polar coupling constant F is given by the usual Fröhlich expression

$$F^2 = \frac{\hbar\omega_{\text{LO}}}{4}\left(\frac{1}{\epsilon_\infty} - \frac{1}{\epsilon_0}\right) \tag{5}$$

where ϵ_∞ and ϵ_0 are the optical and static dielectric constants, respectively. The sum in (3) extends over all bands ν' and over all phonons wave vectors $\boldsymbol{q}$ in the first BZ. This implies that for some of the phonon wave vectors $\boldsymbol{q}$, a nonzero $\boldsymbol{G}$ is required to bring $\boldsymbol{k}'$ into the first BZ. This corresponds to the inclusion of Umklapp processes. Piezoelectric scattering (i.e., the polar electron-acoustic phonon interaction) has been ignored. The numerical integration over the energy-conserving delta function is done using an algorithm proposed by Gilat and Raubenheimer [23]. The same technique is employed during the MC simulations to select the final state of the carriers after a collision [2]. The electron–phonon matrix element has been approximated by an isotropic coupling constant $\Delta_\eta \boldsymbol{q}$ (η = longitudinal acoustic, LA, and transverse acoustic, TA) or $(\Delta K_{op})_\eta$ (η = longitudinal optical, LO, and transverse optical, TO). The acoustic phonon dispersion has been approximated by

$$\hbar\omega_{\eta,\boldsymbol{q}} = \hbar\omega_{\eta,\max}\left[1 - \cos\left(\frac{qa}{4}\right)\right]^{1/2} \tag{6}$$

(where $\omega_{\eta,\max} = 4c_\eta/a$, with c_η the sound velocity with polarization η, is some average phonon frequency at the edge of the BZ, in fair agreement with the spectra of [22]) for $q < 2\pi/a$, a being the lattice constant, while $\hbar\omega_{\eta,\boldsymbol{q}} = \hbar\omega_{\eta,\max}$ for $q \geq 2\pi/a$. The error by a factor $2^{1/2}$ implied by (6) at low phonon frequency has been already discussed in [2]. The dispersion of the optical phonons has been ignored, as usual, and their energy has been taken from the literature [22]. The values of the coupling constants Δ_η have been obtained by fitting the results of Monte Carlo runs in uniform field to experimental data of velocity–field characteristics, as illustrated below.

TABLE I
LOCAL PSEUDOPOTENTIAL FORM FACTORS (Ry)

	a(Å)	$V_S(G^2=3)$	$V_S(G^2=8)$	$V_S(G^2=11)$	$V_S(G^2=3)$	$V_A(G^2=4)$	$V_A(G^2=11)$	E_{cutoff}
Ge	5.65	−0.238	0.0038	0.068	—	—	—	6
Si[a]	5.43	−0.224	0.055	0.072	—	—	—	8
GaAs	5.64	−0.23	0.01	0.055	0.07	0.05	0.01	6
InP	5.86	−0.265	0.01	0.060	0.07	0.05	0.01	6
AlAs	5.66	−0.22	0.043	0.060	0.013	0.055	0.02	6
InAs[b]	6.04	−0.22	0.0	0.05	0.08	0.05	0.03	6
GaP[b]	5.44	−0.22	0.03	0.07	0.12	0.07	0.02	6

[a]Local form factors given in [21].
[b]From [3].

C. Impact Ionization

Impact ionization has been simulated using the Keldysh expression [16]–[19]

$$\frac{1}{\tau_{ii}(E)} = \frac{P}{\tau_{op}(E_{\text{th}})}\left(\frac{E - E_{\text{th}}}{E_{\text{th}}}\right)^2 \tag{7}$$

$1/\tau_{ii}(E)$ being the ionization rate for an electron having energy E larger than a threshold energy, E_{th} · $1/\tau_{op}(E_{\text{th}})$ is the electron-optical phonon scattering rate averaged over all electron wave vectors corresponding to the threshold energy E_{th}, and P is a coupling constant. We have already expressed our skepticism about the quality of (7) in our context [2]. Recently, the effect of anisotropic thresholds on the empirical parameters E_{th} and $P/\tau_{op}(E_{\text{th}})$ has been studied by the NTT group with an improved but still empirical formalism [24]–[26], as we shall discuss.

D. Alloy Scattering

We have treated alloy scattering following Harrison and Hauser [27] for completely random alloys, as implemented by Hauser and co-workers [14] for III–V alloys. We have accounted for the wave-vector dependence of the change of carrier energy in an alloyed material, as suggested by Singh and Bajaj [28], and for the pseudopotential density of states

$$\frac{1}{\tau_{\text{alloy}}(\boldsymbol{k})} = \frac{3\pi^3}{16\hbar}x(1-x)\Omega\left|\Delta E_{\text{alloy}}(\boldsymbol{k})\right|^2 \mathfrak{D}[E(\boldsymbol{k})] \tag{8a}$$

where

$$\Delta E_{\text{alloy}}(\boldsymbol{k}) = E_{AC}(\boldsymbol{k}) - \chi_{AC} - E_{BC}(\boldsymbol{k}) + \chi_{BC}. \tag{8b}$$

Here, χ_{AC} and χ_{BC} are the electron affinities of the binary compounds constituting the alloy $A_xB_{1-x}C$, x is the mole fraction of the compound AC, $\Omega = a^3/4$ is the volume of the primitive cell, and $\mathfrak{D}[E(\boldsymbol{k})]$ is the density of states of the alloy, as obtained from the interpolated band structures of the compounds AC and BC, (2). This expression, also used by Al-Omar and Krusius [29], [30], is the small-k limit of the more general expression given by Marsh [32] for a nonrandom alloy distribution. Quite frankly, the only reason for preferring a random alloying to Marsh's expression is the complexity of his formula when the band structure must be interpolated numerically. With the electron affinities given in [22], the inclusion of alloy scattering for the determination of the velocity–field characteristics in $Al_{0.5}Ga_{0.5}As$ and in $In_{0.53}Ga_{0.47}As$ caused small changes comparable with the uncertainty and the scatter of the experimental data. Therefore, no conclusions can be drawn about the validity of our formulation.

E. Coulomb Interactions

The homogeneous simulations dealt with in this paper have been performed without any Coulomb scattering (i.e., neither ionized impurity nor intercarrier), since most experimental data have been obtained in pure, intentionally undoped materials. The treatment of these processes in a device simulation context has been presented in great detail in [2]. We shall only add that, in the case of holes in Si, the overlap integrals occurring in the hole-phonon and intercarrier collisions have been treated with a four-bands $\boldsymbol{k}\cdot\boldsymbol{p}$ approximation, much in the same way as in [30], [31].

III. BAND STRUCTURE

In Table I we list the pseudopotential form factors used to generate the conduction-band structures of the seven compounds, shown in Fig. 1 together with the valence-band structure of Si. Also shown in Table I are the lattice constants, as well as the cutoff energies E_{cutoff} (in Rydbergs) related to the number of plane waves $\exp(i\boldsymbol{G}\cdot\boldsymbol{r})$ used for every $\boldsymbol{k}$: plane waves such that

$$\frac{\hbar^2}{2m_0}(\boldsymbol{k}+\boldsymbol{G})^2 \le E_{\text{cutoff}} \tag{9}$$

(where m_0 is the free electron mass) were considered. Typically, we have tried to adhere as much as possible to the values given in [3]. In most cases, however, we had to adjust the Cohen–Bergstresser values for two reasons: 1) In the tabulation of the band structure for $\boldsymbol{k}$ over the irreducible wedge, we had to strive for smoothness. Using a small number of plane waves, such as about 20, as in [3], we found significant discontinuities for the eigenvalues $E_\mu(\boldsymbol{k})$, as the sphere defined by (9) includes a variable number of $\boldsymbol{G}$ vectors (thus yielding a variable rank of the matrix to invert), as $\boldsymbol{k}$ moves in the wedge. A larger number of plane waves is needed to minimize the size of the discontinuities. Since the *empirical* pseudo-potentials given by Cohen and Bergstresser provide a good fit to experimental data only when their procedure is followed *exactly* (i.e., using the same number of plane waves), we had to check for the quality of the fit as the number of plane waves was increased to 80–90 (III–V's and Ge) or to 110–120 (Si). In the particular case of AlAs, no form factors are given in [3] and [21] and we had to derive them. The values for the energies of transitions between various symmetry points which have been used for fitting the form factors are from [3], [21], and [22]. 2) While the Cohen–Berg-

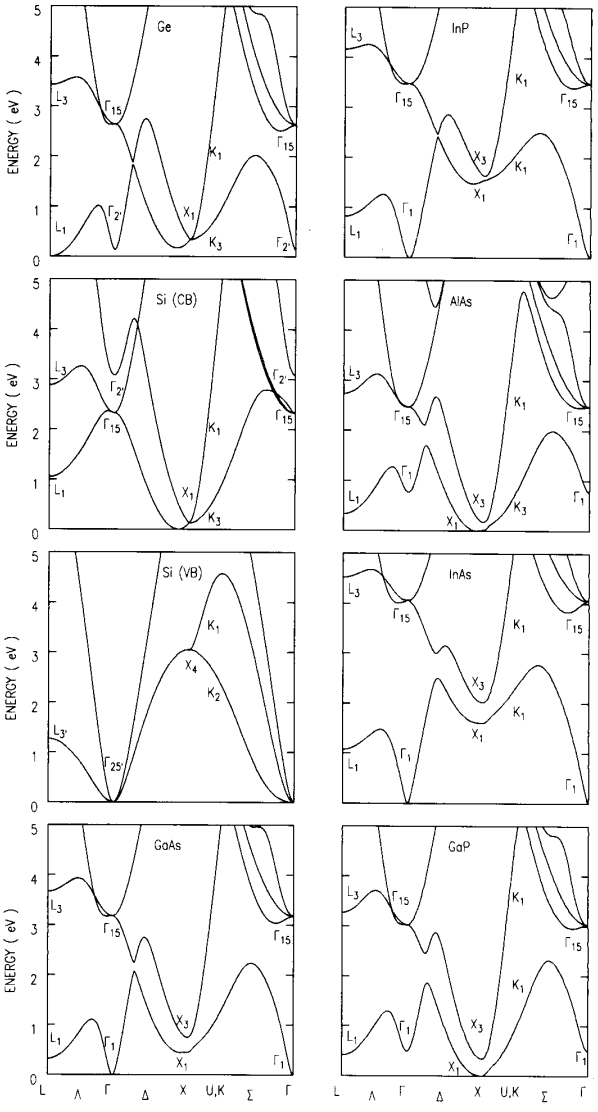

Fig. 1. Band structures obtained from the empirical pseudopotential form factors listed in Table I. Energies are measured from the bottom of the conduction band, except for the case of the Si valence band, where energies are measured downwards from the top at the Γ point.

stresser form-factors provide a good fit to large-scale features of the bands (i.e., on the energy scale of several tenths of electronvolts), high-field electron transport depends crucially on finer details of the band structure (e.g., the Γ–L energy splitting for GaAs could vary between 0.2 and 0.4 eV without affecting significantly the quality of the fit for higher energy transitions). The improved experimental knowledge of the conduction-band structures of many materials since 1966 is reflected in a slightly different choice of the form factors, particularly for Ge, GaAs, and InP. For Si, we have chosen the local form factors given by Chelikowsky and Cohen [21], as they give much better fits for the effective mass at the minimum along the symmetry line Δ and for the bandgap energy. Thus we employed the values prescribed by [3] only in the case of InAs and GaP.

We list in Table II some important band-structure-related parameters extracted from our pseudo-potential calculations: the energies at the symmetry points Γ, L, X, and X_3, the effective masses (along the longitudinal l and transverse t directions for the L and X minima) in units of the free electron mass m_0, the location of the minimum along the symmetry line Δ, and the nonparabolicity parameter α, which we define from the first-order $\boldsymbol{k} \cdot \boldsymbol{p}$ expansion as

$$\frac{\hbar^2 \boldsymbol{k}^2}{2m^*} = E(\boldsymbol{k})\left[1 - \alpha E(\boldsymbol{k})\right] \tag{10}$$

where m^* is the effective mass at the bottom of the valley. We note a few significant departures we have taken away from the more "customary" values used by other authors [34]–[37] (listed for convenience in Table III, where the label d denotes the density-of-states effective mass):

1) The nonparabolicity parameter for the Γ valley of GaAs has been determined accurately by Heiblum and co-workers [38], [39]. The value is significantly larger than commonly employed [33].

2) In previous MC simulations of electron transport in InP, the L-valley minimum has been consistently assumed to lie some 0.4 to 0.6 eV above the Γ minimum [12]–[14], [20]. However, recent optical measurements have placed it significantly higher (about 0.86 ± 0.04 eV) [34]. The choice of the form factors for InP in Table I reflects this new information. As pointed out by Herbert *et al.* [13], this results in a higher value for the effective mass at the L-valley minimum as well.

It should also be noted that, in most cases, the minimum along the symmetry line Δ is strongly nonparabolic. In the case of AlAs and GaP, a camel's back structure (not reproduced by our calculations for GaP) has been observed [22], the longitudinal effective mass being an ill-defined quantity. It is enough to point out the wide scatter of data for $m_X(l)$ in GaP, ranging from 0.87 m_0 to 7.25 m_0, as the various experimental techniques probe the mass at different distances from the camel's back at X. Also for Ge, GaAs, and InP, the dispersion along the Δ line is very flat near the minimum, getting steeper as we move away towards Γ. Moving along Δ, but in the opposite direction, towards the X symmetry point, the dispersion gets steeper at first, but then flattens out once more, as we approach the X symmetry point. Thus the values for the longitudinal effective masses are somewhat arbitrary, depending on the discretization used to numerically compute the second derivative of the dispersion close to the valley minimum. This is also indicated by the large (and positive!) nonparabolicity parameters shown in Table II. For some materials (particularly InP), a similar situation is found at the L-symmetry point. The values for the effective masses listed in Table II are computed using a step of 0.01 ($2\pi/a$). Nonparabolic corrections have been computed at approximately 0.1 eV (or sometimes less) above the local minimum, in order to keep second-order corrections (ignored in (10)) to a few parts in 10^2 in the worst case. Fig. 2 shows the density of states obtained from the bands of Fig. 1 using the Gilat–Raubenheimer algorithm [23]. Finally, we show in Fig. 3 the energies at the symmetry points E_Γ, E_L, E_X, and E_{X_3} as a function of alloy composition for $Al_xGa_{1-x}As$, $In_xGa_{1-x}As$, and $Ga_xIn_{1-x}P$. A constant bowing has been employed throughout. Note how the values of the mole fraction x for transitions from direct to indirect gap are fairly consistent with experimental results (see, for example, [22]). Note also the importance of including the second conduction band (X_3) for a large x in $Ga_xIn_{1-x}P$ and $Al_xGa_{1-x}As$.

TABLE II
BAND-STRUCTURE PARAMETERS

	E_{gap}(eV)[a]	E_Γ(eV)[b]	E_L(eV)[b]	E_Δ(eV)[b,c]	E_{X_3}(eV)[b]	$m_\Gamma(m_0)$	α_Γ(eV^{-1})[d]	$m_L(m_0)$	α_L(eV^{-1})	$m_X(m_0)$	α_X(eV^{-1})
Ge	0.744 (77 K) 0.664 (300 K)	0.135	0.0	0.173 (0.83)	—	0.042	−0.85	1.387 (l) 0.101 (t)	−0.33[e]	1.791 (l) 0.204 (t)	2.40 (l) −0.14 (t)
Si	1.21 (77 K) 1.12 (300 K)	2.375	1.049	0.0 (0.85)	—	—	—	1.634 (l) 0.126 (t)	−0.30[e]	0.903 (l) 0.191 (t)	−0.43[e]
GaAs	1.51 (77 K) 1.42 (300 K)	0.0	0.323	0.447 (0.91)	0.747	0.063	−1.16[f]	1.538 (l) 0.127 (t)	−0.40[e]	1.987 (l)[g] 0.229 (t)	−0.55[e,g]
InP	1.42 (77 K) 1.34 (300 K)	0.0	0.832	1.492 (0.85)	1.645	0.082	−0.61	1.878 (l) 0.153 (t)	4.13 (l) −0.49 (t)	1.321 (l) 0.273 (t)	2.70 (l) −0.12 (t)
AlAs	2.22 (77 K) 2.14 (300 K)	0.767	0.333	0.0 (0.90)	0.174	0.149	−1.10	1.386 (l) 0.148 (t)	−0.45[e]	0.813 (l) 0.223 (t)	−0.83[e,g]
InAs	0.418 (77 K) 0.356 (300 K)	0.0	1.078	1.607 (1.00)	2.019	0.031	−2.20	1.565 (l) 0.124 (t)	−0.45[e]	3.619 (l) 0.271 (t)	5.00 (l)[g] −0.14 (t)
GaP	2.35 (77 K) 2.27 (300 K)	0.496	0.415	0.0 (1.00)[h]	—	0.126	−0.51	1.493 (l) 0.142 (t)	−0.21[e]	1.993 (l) 0.250 (t)	1.90 (l)[g] −0.02 (t)

[a]From the compilation in [22].
[b]Measured from the bottom of the conduction band.
[c]In parenthesis the location of the minimum along the symmetry line Δ, in units of $2\pi/a$.
[d]Averaged over (100), (110), and (111) directions.
[e]Averaged over longitudinal and transverse directions.
[f]See [38] and [39].
[g]Due to the camel's back structure or the strong nonparabolicity at X, $\alpha_X(l)$ has been computed only along the (100)-direction towards Γ.
[h]Experiments place the Δ minimum 0.07–0.1 $(2\pi/a)$ away from X.

TABLE III
BAND-STRUCTURE PARAMETERS FROM THE LITERATURE

	E_Γ(eV)	E_L(eV)	E_Δ(eV)	E_{X_3}(eV)	$m_\Gamma(m_0)$	α_Γ(eV^{-1})[d]	$m_L(m_0)$	α_L(eV^{-1})	$m_X(m_0)$	α_X(eV^{-1})
Ge	0.20[a] 0.14[b]	0.0[a]	0.5[a] 0.18[b]	—	0.031 to 0.042[a]	—	1.57–1.74 (l)[b] 0.081 (t)[a,b]	−0.3[b]	1.353 (l)[b] 0.288 (t)[b]	—
Si	2.19 to 2.35[a]	—	0.0[a]	—	—	—	—	—	0.916 (l)[a] 0.191 (t)[a]	−0.5[c]
GaAs	0.0[a]	0.21 to 0.30[a,d,e]	0.36 to 0.48[a,d,e]	0.88[d]	0.067[a]	−0.69[e]	1.47[f]–1.9 (l)[d] 0.075[d]–0.12 (t)[f]	−0.65[e]	1.3–1.9 (l)[a,d,f] 0.19–0.37 (t)[a,d,f]	−0.36[e]
InP	0.0[a]	0.4–0.6[a,g,h] 0.86[k]	0.66 to 0.95[a,h]	—	0.068 to 0.083[a,h]	−0.83[h]	0.26 (d)[h] 0.4 (d)[g]	−0.23[h]	0.325 (d)[h] 0.4 (d)[g]	−0.38[h]
AlAs	0.676[f] to 1.2[a,f,i]	0.182 to 0.32[i,f]	0.0[a]	0.2[a]	0.124 to 0.172[a,f,i]	—	1.47–1.9 (l)[d,f] 0.096–0.16 (t)[d,f]	−0.40[f]	1.1–5.8 (l)[a,f,i] 0.19–0.24 (t)[a,f,i]	−0.36[h]
InAs	0.0[a]	1.082[h] 1.35[f]	1.62[h]	—	0.022 to 0.064[a,h,j]	−1.39[h]	0.286 (d)[h]	−0.54[h]	0.64 (d)[h]	−0.90[h]
GaP	0.51 to 0.58[a]	—	0.0[a]	—	—	—	—	—	0.87–7.25 (l)[a] 0.21–0.39 (t)[a]	—

[a]From the compilation in [22].
[b]From [7].
[c]From [8].
[d]From [33].
[e]From [56].
[f]From [35].
[g]From [13].
[h]From [20].
[k]From [34].
[i]From [36].
[j]From [37].

IV. RESULTS FOR HOMOGENEOUS TRANSPORT

The nonpolar electron-acoustic phonon deformation potential Δ_{ac} the nonpolar electron-optical phonon deformation potential $(DK)_{op}$, the prefactor $P/\tau_{op}(E_{th})$, for the Keldysh ionization rate, and the (isotropic) ionization threshold E_{th} are the scattering parameters to be determined in our transport model. This was accomplished by fitting to experimental data the MC-generated velocity versus electric field characteristics to determine the electron–phonon coupling constants, and ionization rates versus electric field to determine the two ionization parameters. As stated previously [2], the uniqueness of the solution to this

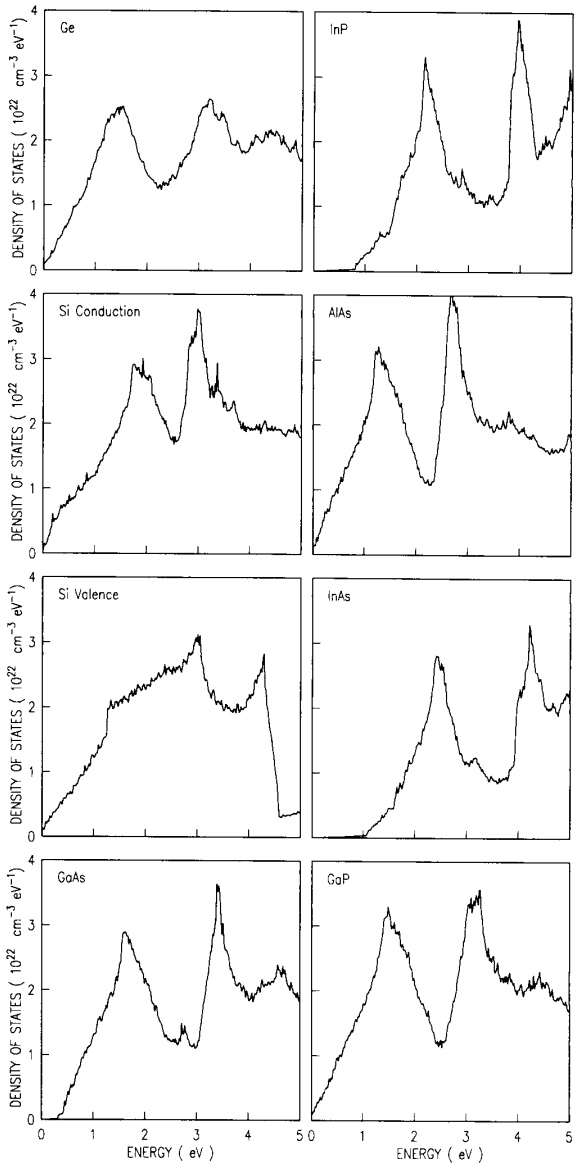

Fig. 2. Density of states derived from the band structures of Fig. 1.

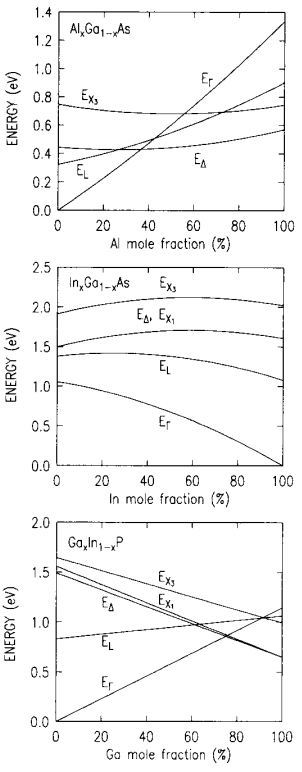

Fig. 3. Variations of the energy of satellite valleys in III–V ternary alloys as a function of alloy composition obtained from a linear interpolation. Constant bowing parameters (0.26 eV for $Al_xGa_{1-x}As$ and -0.6 eV for $In_xGa_{1-x}As$, from [22]) have been used. Zero bowing has been used for $Ga_xIn_{1-x}P$.

"fitting" problem is highly questionable. On the one hand, some of the experimental data are relatively insensitive to some of the scattering parameters we are trying to determine, such as the Γ-to-L deformation potential in GaAs based on the velocity–field characteristics. On the other hand, other data depend globally on the whole set of coupling constants, such as impact ionization. Therefore, minor differences (of the order of 20% or less) between the results presented here and those reported in the literature should not be considered to be significant.

We have made a few major approximations: We have lumped LO and TO phonons into a single process (which we still label "LO"). Moreover, since the electron-TA phonon coupling vanishes at the Γ point, we have ignored this process for all materials, except for Si and Ge. The error made in instances where this process is effective (GaP, AlAs, even at very low fields, and in all materials at high fields as the wave vectors of most carriers are away from high-symmetry points) is probably small, considering the strength of additional processes, particularly the polar electron-LO phonon scattering in the polar III–V compounds.

Table IV lists the values of the empirically determined constants, and of other quantities we used to compute the scattering rates. Fig. 4 shows the total electron–phonon scattering rate as a function of kinetic energy above the conduction-band minimum (or below the valence-band maximum in the case of hole-phonon rates in Si) at two temperatures. This "averaged" scattering rate, $1/\tau_{el\text{-}ph}(E)$, is obtained from the anisotropic scattering rate $1/\tau_{\eta,\mu}(\boldsymbol{k})$, for a carrier in band μ with wave vector $\boldsymbol{k}$, by summing over all the bands μ, phonon processes η, and averaging over the density of (initial) states of energy E

$$\frac{1}{\tau_{el\text{-}ph}(E)} = \frac{1}{\mathfrak{D}(E)} \sum_{\mu,\boldsymbol{k},\eta} \frac{1}{\tau_{\eta,\mu}(\boldsymbol{k})} \delta[E_\mu(\boldsymbol{k}) - E] \quad (11)$$

where $\mathfrak{D}(E)$ is the density of (initial) states at every E. The strong influence of the density of final states is clearly evident, comparing the qualitative shape of the curves in Fig. 2 to Fig. 4.

A comparison between the deformation potentials listed in Table IV and those used previously in the literature is complicated by the many band-structure considerations we have discussed above and in [2]. Nevertheless, it is interesting to com-

TABLE IV
SCATTERING PARAMETERS

	Δ_{ac} (eV)[a]	$(DK)_{op}$ (10^8 eV/cm)[a]	P/τ (10^{13} s^{-1})[a]	E_{th} (eV)[a]	ϵ_0[b]	ϵ_∞[b]	$\hbar\omega_{op}$ (meV)[b]	c_s (10^5 cm/s)[b]	ρ (g/cm^3)[b]
Ge	2.5	3.5	2.0	E_{gap}	16.0	—	37.04	5.4 (l) 3.2 (t)	5.32
Si	1.2 (band 1) 1.7	1.75 (band 1) 2.1	0.01	E_{gap}	11.7	—	62.00	9.18 (l) 4.70 (t)	2.33
GaAs	5.0	2.10	250.0	E_{gap} + 0.3	12.90	10.92	35.36	5.24 (l) 2.47 (t)	5.36
InP	5.0	2.0	15.0	E_{gap} + 0.35	12.61	9.61	42.40	5.13 (l) 3.10 (t)	4.81
AlAs	7.0	2.0	—	—	10.06	8.16	50.09[c]	5.65 (l)[c] 3.90 (t)[c]	3.76[c]
InAs	5.8	2.0	0.25	0.454 (77 K) 0.383 (300 K)	15.15	12.75	30.08	4.28 (l) 2.65 (t)	5.67
GaP	5.0	1.0	—	—	11.10	9.08	45.23	5.84 (l) 4.13 (t)	4.14

[a]From present Monte Carlo simulations.
[b]From the compilation of [22].

pare the strength of the various intervalley processes. We should stress that in our case we do not have the freedom to vary the various deformation potentials independently, once Δ_{ac} and $(DK)_{op}$ have been determined. We can still define an "effective" intervalley deformation potential $(Dq)_{ij}$ and the energy of the relative phonon $\hbar\omega_{ij}$, assisting the transition from valley i to valley j, by adding all possible contributions (LO, LA and, when available, TA) as follows:

$$(Dq)_{ij}^2 = (\Delta_{LA} q_{ij})^2 + (\Delta_{TA} q_{ij})^2 + (DK)_{op}^2 \tag{12a}$$

$$1/\hbar\omega_{ij} = \left[(\Delta_{LA} q_{ij})^2/\hbar\omega_{LA}(q_{ij}) + (\Delta_{TA} q_{ij})^2/\hbar\omega_{TA}(q_{ij}) + (DK)_{op}^2/\hbar\omega_{LO}\right]/(Dq)_{ij}^2, \tag{12b}$$

so that $(Dq)_{ij}^2/\hbar\omega_{ij}$ represents the effective strength of the intervalley process for emissions at zero temperature. Here q_{ij} is the magnitude of the phonon wave vector connecting the valley minima, while $\hbar\omega_\eta(q_{ij})$ is the dispersion of mode η, obtained under the approximation of (6). In Table V we list the values we obtain from Table IV and (12). Note that similar tables in [2] are slightly different, since there a correction of a factor $2^{1/4}$ was made to the acoustic deformation potential in order to partially compensate the low-frequency error in (6). This correction has not been used here. Also shown is a collection of deformation potentials used in the MC literature [7], [11], [13], [14], [20], [40]. A complete discussion of the intervalley deformation potentials is outside the scope of this work. It is enough to stress that our values are consistently lower than those employed in previous MC simulations, as a glance at Table V shows. Lower values are indeed generally predicted by pseudopotential calculations, as in, for example, [41]–[44], and from some experimental data "chosen" from the still controversial literature [40], [45], [46]. The oversimplified band structure used in "conventional" MC simulations may be at the origin of this difference. As an example, Table V shows that differences are seen acutely for the X–X transitions. The higher density of states induced by the camel's back structure and/or the strong nonparabolicity along the longitudinal direction are going to increase the scattering rate, while keeping $(Dq)_{XX}$ fixed. A lower deformation potential is needed in order not to overestimate the intervalley transition rate when the "correct" band structure is included in the MC simulation. For ternary alloys, the scattering rates are obtained from a simple linear interpolation of the deformation potentials in Table IV, while the impact ionization parameters must be independently determined from a fit to experimental data (when available). We shall now discuss the various results of our homogeneous, steady-state simulations as compared to experimental data.

A. Velocity–Field and Energy–Field Characteristics

Figs. 5 and 6 show the velocity–field and energy–field characteristics for electrons in Ge, Si, GaAs, InP, and holes in Si at 77 and 300 K, and for electrons in three ternary alloys ($Al_xGa_{1-x}As$, $In_xGa_{1-x}As$, and $Ga_xIn_{1-x}P$) at 300 K, with mole fraction x as a parameter.

In the case of Si and Ge, the simulations have been performed for two orientations of the electric field (along the (100) and (111) directions), and have been compared with experimental data for electrons in Ge [7], and electrons [4] and holes [5] in Si. Interesting features, such as negative differential mobilities (also predicted for the case of 300 K electrons in Si by [25], [26]) and/or sharp rises of the characteristics are seen at fields too large to be experimentally accessible.

The case of III–V materials is more interesting, as the experimental data are incomplete and show significant scatter. For GaAs, our MC simulations predict the peak velocity to occur at a field strength of about 5 kV/cm at 300 K, in agreement with the data by Masselink and Braslau [47], but higher than the value of 3.5 to 4 kV/cm reported by Ruch and Kino [48], which is also normally obtained in other MC simulations [11], [20]. This is consistent with the higher Γ–L deformation potential employed elsewhere. At high fields, a decreasing velocity is predicted, as seen experimentally [49]–[51]. Our low-temperature results reproduce the features observed in [47], but predict a slightly lower peak velocity. The experimental situation for InP is quite uncertain, as high-field data from Windhorn and co-workers [52] on one side, and from Boers [53] and Robson and co-workers [54] on the other side, are in disagreement. We

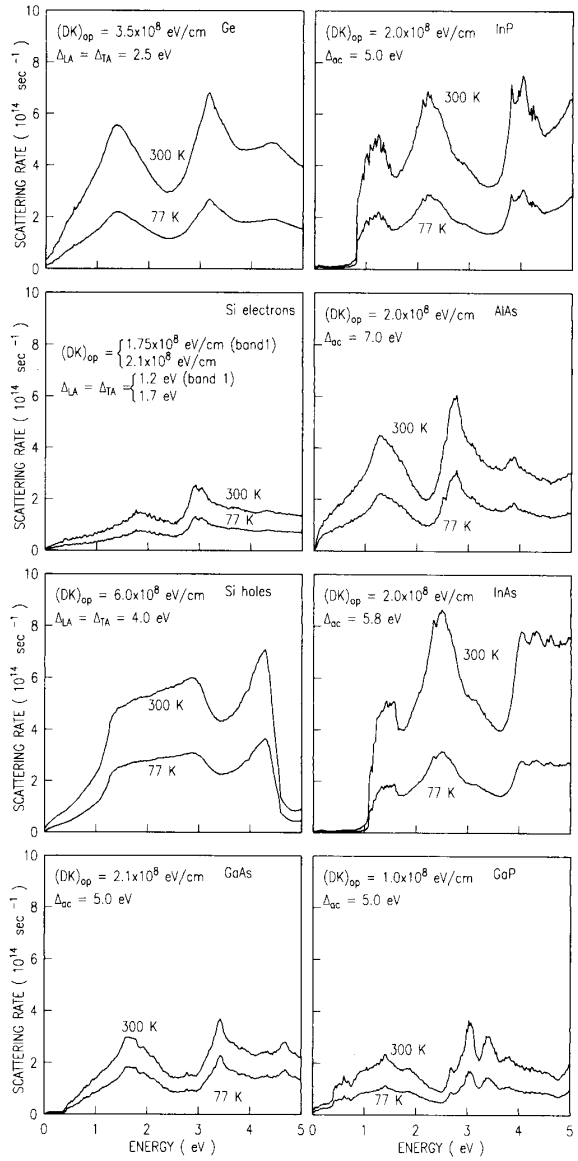

Fig. 4. Carrier-phonon scattering rates at 77 and 300 K averaged over equi-energy surfaces for the semiconductors of Figs. 1 and 2. The deformation potentials used for hole transport in Si (not listed in Table IV) are also indicated.

have preferred the more recent results of [52]. A Γ-L intervalley deformation and an acoustic-phonon deformation potential in L much higher than those we chose are needed to match the data of [53] and [54]. A lower Γ-L energy splitting would not help, but it would reduce the value of the field at which the peak velocity is reached, about 12 kV/cm in our simulations, which is in excellent agreement with the experimental data reported by Majerfeld and co-workers [55]. Not much is known experimentally about bulk $Al_xGa_{1-x}As$, as attested by the theoretical exploratory work by Brennan and Hess [56]. The value for the acoustic deformation potential in Table IV for AlAs has been extracted from the literature [22], while the optical deformation potential has been assumed to be similar to other III–V materials. The $Al_xGa_{1-x}As$ velocity-field characteristics shown in Fig. 4 are obtained by the linear interpolation of the scattering parameters of Table IV between GaAs and AlAs. Experimental work on bulk $Al_xGa_{1-x}As$ is needed before we can draw any conclusion, as also stated by Brennan and Hess [56].

The theory of velocity-field characteristics of InAs is strictly linked to its impact-ionization properties, because of its small bandgap. The situation is intriguing: The possibility of the existence of a region of negative differential mobility (NDM) was proposed by Matz, [57], on the grounds of the strong nonparabolicity of the Γ valley in this material. Later, Fawcett and coworkers [37] used MC simulations to show that nonparabolicity cannot yield any NDM. They concluded that impact ionization prevents the electrons from "running away" at the energies necessary to trigger intervalley transitions, so that no NDM should be seen. Brennan and Hess [20] confirmed this view. Information about intervalley transfer was obtained by Kuchar and co-workers [58], who observed a negative differential conductivity in a strong magnetic field. Recently, NDM has been observed directly at 77 K by Dobrovl'skis and colleagues [59]. By using short pulses to prevent impact ionization before its onset at a field of about 1 kV/cm [60], [61], NDM was seen at a field of about 2 kV/cm at 77 K, but not when using longer pulses. This is consistent with the established idea that impact ionization "hides" the NDM by preventing the carriers from running away and undergoing intervalley transitions. Unfortunately, the lack of purity of the samples in [59] distorts the low-field characteristics by depressing the mobility. We summarize the situation in Fig. 7, comparing the results of our simulations, with and without impact ionization, to experimental and theoretical curves. Our simulations without impact ionization predict correctly both the peak field and the peak velocity of [59], giving us some confidence about the intervalley scattering rates we have employed. Further confidence is gained looking at our results for the InP-lattice-matched $In_{0.53}Ga_{0.47}As$ shown in Fig. 5 and, in more detail, in Fig. 8. The figures show that a simple interpolation between InAs and GaAs band structures and scattering parameters provides a remarkable agreement with the experimental low-field data by Marsh [32] and high-field data by Windhorn and co-workers [62], [63]. Note how a crossover between the high-field drift velocity in GaAs and $In_{0.53}Ga_{0.47}As$ in Fig. 5 is predicted to occur at about 15 to 20 kV/cm, in excellent agreement with the experimental value of about 20 kV/cm [62], [63]. Unfortunately, we remain puzzled by a serious inconsistency: If we ignore $\boldsymbol{k}$-dependent bowing effects in the interpolation of the band structures of InAs and GaAs, we obtain a value of about 0.75 eV for the Γ-L energy splitting $\Delta E_{\Gamma,L}$. Similar values are obtained from other pseudopotential [64] and $\boldsymbol{k} \cdot \boldsymbol{p}$ calculations (see [65, Fig. 3], while an even larger value ($\simeq$ 0.89 eV) is obtained from the $\boldsymbol{k} \cdot \boldsymbol{p}$ calculations of [64]. On the contrary, $\Delta E_{\Gamma,L}$ has been measured to be 0.55 eV [66] by ultraviolet photoemission. We cannot account for the excellent agreement between MC simulations and experiments shown in Figs. 5 and 8, in view of the result of [66]. As far as GaP is concerned, very little is known experimentally. What little is known is confusing. Low-field mobilities as high as 190 $cm^2/V \cdot s$ have been measured [22]. Velocity-field characteristics have also been measured [67] and modeled [68]. A saturated velocity somewhat larger than 10^7 cm/s has been observed in samples which showed a significantly lower ohmic mobility (about 83 $cm^2/V \cdot s$). We have chosen to compromise, by assuming the higher mobility is correct (there can be

TABLE V
INTERVALLEY SCATTERING PARAMETERS

	This Work $(Dq)_{ij}$ (10^8 eV/cm) and $\hbar\omega_{ij}$ (meV)[a]					Previous Work $(Dq)_{ij}$ (10^8 eV/cm) and $\hbar\omega_{ij}$ (meV)				
ij =	ΓL	ΓX	LL	LX	XX	ΓL	ΓX	LL	LX	XX
Ge	4.88 (23.21)	4.78 (23.04)	5.26 (23.95)	4.65 (22.83)	3.78 (30.71)	2.00[b] (27.56)	10.0[b] (27.56)	3.00[b] (27.56)	4.06[b] (27.56)	9.46[b] (37.04)
Si	—	—	2.63 (38.87)	2.34 (37.16)	2.26[c] (50.90)	—	—	—	—	—[c]
GaAs	5.25 (22.69)	5.48 (23.45)	5.94 (24.97)	5.01 (21.85)	2.99 (24.31)	6.50[d] (27.80)	10.0[e] (29.9)	10.0[e] (29.0)	5.00[e] (27.8)	7.06[e] (29.90)
						10.0[f] (26.0)	10.0[f] (26.0)	10.0[f] (26.0)	9.00[f] (26.0)	9.00[f] (26.0)
InP	5.06 (22.15)	4.98 (21.89)	5.75 (24.27)	4.68 (20.90)	2.80 (25.68)	4.40[g] (33.60)	4.30[g] (33.6)	2.46[g] (33.6)	3.67[g] (42.2)	4.60[g] (23.94)
						10.0[f] (27.8)	10.0[f] (29.9)	10.0[f] (29.0)	9.00[f] (29.3)	9.00[f] (29.9)
AlAs	7.02 (25.07)	7.30 (25.07)	8.02 (26.97)	6.63 (23.24)	3.57 (26.34)	—	—	—	—	—
InAs	5.59 (17.45)	6.35 (19.23)	6.35 (19.23)	5.59 (17.45)	3.36 (19.26)	10.0[f] (27.80)	10.0[f] (29.9)	10.0[f] (29.0)	9.0[f] (29.3)	9.0[f] (29.9)
						5.0[h]		10.0[h]		
GaP	5.10 (25.56)	5.86 (28.56)	5.86 (28.56)	5.10 (25.56)	2.77 (26.61)	—	—	—	—	—

[a]In parenthesis.
[b]From [7]. An X-X g process of strength 0.79×10^8 eV/cm assisted by an 8.61-meV phonon and an L-L process of strength 0.2×10^8 eV/cm assisted by a 10.34-meV phonon were also used.
[c]See [2] for a discussion of various f and g processes compared with values used in previous Monte Carlo simulations.
[d]From [40].
[e]From [11].
[f]From [20].
[g]From [13]. Other weaker intervalley processes were also included.
[h]From [14].

many sample-dependent reasons for observing a lower mobility!) and aiming at a saturated velocity of about 10^7 cm/s. Fig. 9 shows our results at 300 K, while the velocity–field characteristics for $Ga_xIn_{1-x}P$, also at 300 K, are shown in Fig. 5. These results must be considered no more than a working hypothesis. We must wait for a more complete experimental picture before we can fix with sufficient confidence the carrier-lattice coupling constants.

Finally, in Fig. 6 we show the average energies versus electric field for the materials in Fig. 5. Whenever possible, we have compared our results with results of other MC simulations. Two observations must be made: First, note the different energies predicted at high fields by our model and the model developed by Hess and co-workers [17], [18] for electrons in Si. Secondly, the behavior of $In_xGa_{1-x}As$ at high fields is interesting. At small x (i.e., GaAs-like) the average energy is relatively low, due to the presence of the low-lying satellite valley at L. As the InAs mole fraction increases, the L-valley minimum is pushed to a higher energy and higher average energies are seen. When we reach the InAs-like composition, impact ionization sets in, effectively reducing the average energy the electrons can gain at high fields.

B. Impact Ionization

The use of the empirical-pseudopotential band structure gives us some confidence that we can study reasonably well high-energy processes such as impact ionization [16], [17]. However, the use of the Keldysh formula, (7), leaves much to be desired. It is based on the assumption of parabolic bands, direct gap, and it ignores the anisotropy of the ionization threshold. This last effect, considered by the NTT group [24]–[26], could explain the "hard" and "soft" threshold obtained when using (7) for materials with small (e.g., for GaAs) or large (e.g., for Si) anisotropies for E_{th}, respectively. More importantly, (7) neglects phonon-assisted process, which may loosen the requirements imposed by momentum conservation for carriers near threshold. Considering the formidable efforts which would be needed to account for these effects, we shall simply adopt an empirical approach, and refer the readers to the works by Kane [69] and the review by Capasso [70] for a deeper understanding of these issues.

Fig. 10 and Table IV show the results we have obtained for the impact-ionization coefficient α in a few materials, and the values of the parameter $P/\tau_{op}(E_{th})$ (abbreviated as P/τ in the Table and the figure). A satisfactory agreement can be obtained with experimental data ([71], [72] for Ge, [73]–[75] for electrons in Si, [76] for holes in Si, [77]–[79] for GaAs, [80]–[84] for InP, [85] for $In_xGa_{1-x}As$) in almost all cases. InAs is again an exception. Despite the many attempts, as in [60], [86], only one complete measurement of the dependence of α on the field has been reported [87]. Unfortunately, this complete piece of information is inconsistent with a wealth of data showing that onset of ionization occurs at a field of about 1 kV/cm [60], [61], [86], unlike the 40 kV/cm or so reported by Mikhailova

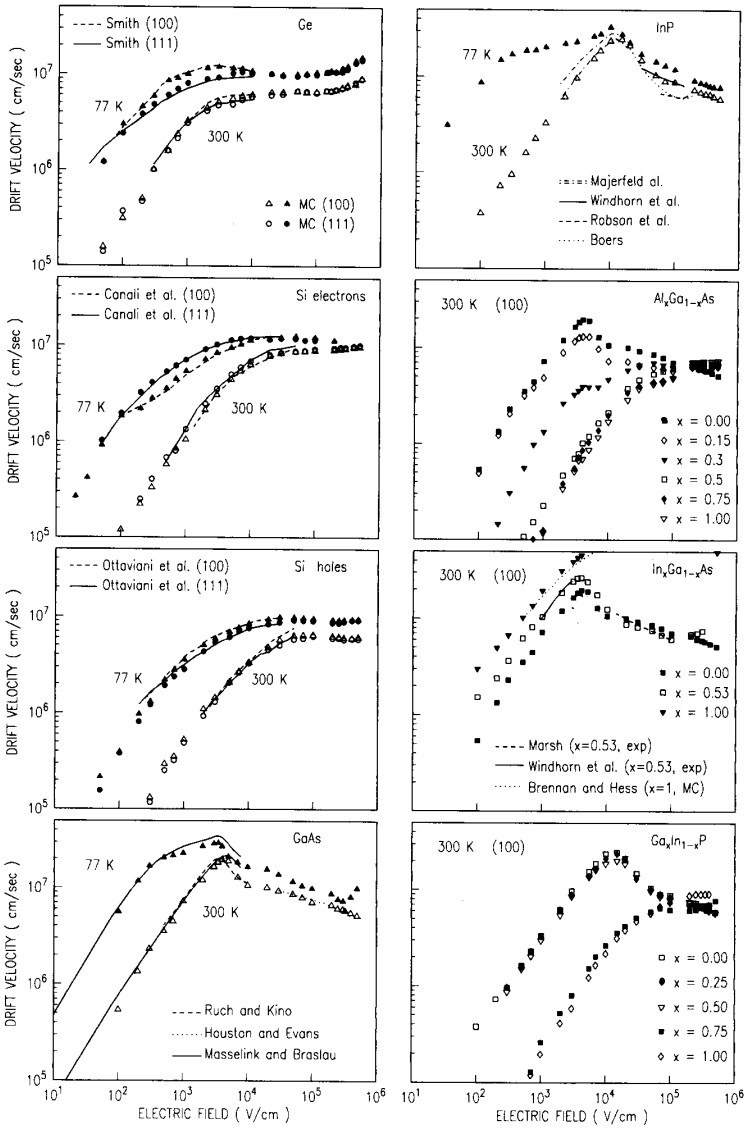

Fig. 5. Calculated carrier drift velocity as a function of electric field at 77 and 300 K for various semiconductors and alloys. Available experimental data are shown for comparison. Note, in the case of InP, that the range of the low-field data reported by Majerfeld [55] is also shown.

and co-workers [87]. Thus we are left without any reliable experimental information. With a threshold computed from the Anderson–Crowell procedure [88], using a small prefactor P/τ for (7), in order to reproduce the room-temperature MC results [20], we have obtained the data shown in Fig. 11. As noted by Brennan and Hess [20], the shrinkage of the InAs bandgap at high temperatures overcomes the cooling of the carriers due to increased phonon scattering. Thus α anomalously increases at higher temperatures. The effect is much larger in our simulations than in those of [20]. Finally, no attempt has been made to simulated impact ionization in AlAs and GaP, due to the uncertainty of the electron–phonon scattering rates and the lack of impact-ionization data.

C. Diffusivities and Relaxation Times

Longitudinal and transverse electron diffusion constants D_l and D_t, respectively, and energy- and momentum-relaxation times τ_w and τ_p, respectively, are shown in Figs. 12 and 13 for Ge, Si, and GaAs. The diffusivities have been computed as in [6]: For the longitudinal diffusion constant we have

$$D_l = \frac{1}{2}\frac{d}{dt}\left\langle \left[x_l(t) - \langle x_l(t)\rangle\right]^2 \right\rangle \tag{13a}$$

where $x_l(t)$ is the displacement along the direction parallel to the external field at time t, and the brackets $\langle \cdots \rangle$ denote the

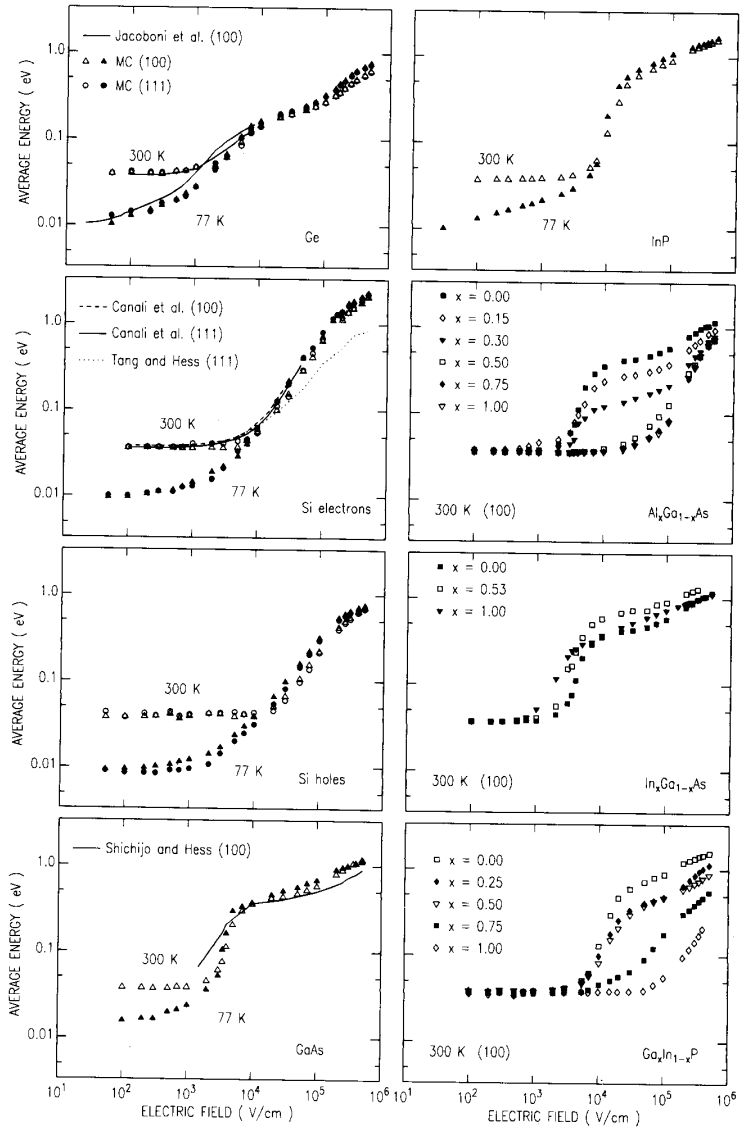

Fig. 6. Calculated carrier average energy as a function of electric field at 77 and 300 K for various semiconductors and alloys. In the case of electrons in Ge, Si, and GaAs, results of previous MC simulations are also shown for comparison.

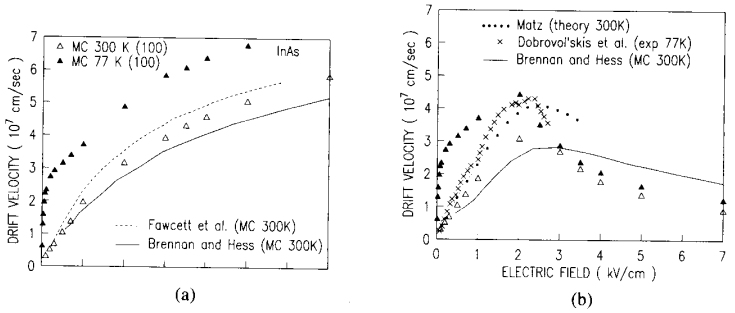

(a) (b)

Fig. 7. Electron drift velocity at low electric fields in InAs (a) with and (b) without impact ionization according to our results and previous work.

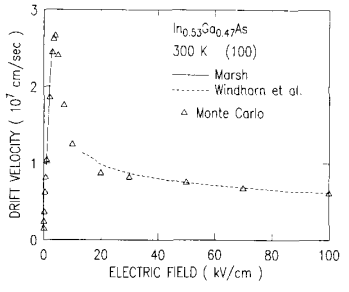

Fig. 8. Electron drift velocity at low electric fields in $In_{0.53}Ga_{0.47}As$ at 300 K from our simulations, from the low-field experimental data by Marsch [32] and from the high-field experimental data by Windhorn and colleagues [62], [63]. Alloy scattering has a minor effect on the results.

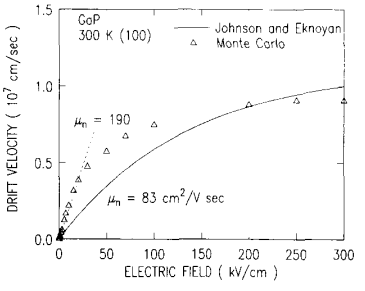

Fig. 9. Electron drift velocity at low electric fields in GaP at 300 K from our simulations and from the experimental low-field mobility reported in [22] is also shown.

ensemble average. In the actual evaluation of (13a) during the MC simulation, we have considered both the ensemble and time average of the time derivative, starting at times long enough for the diffusion law to hold true [6], [9]. Making this averaging and the time-derivative explicit

$$D_l = \frac{1}{N_t N_{pt}} \sum_{i=1}^{N_t} \sum_{p=1}^{N_{pt}} \{x_{l,p}(t_i) v_{l,p}(t_i) - v_d x_{l,p}(t_i) - v_d v_{l,p}(t_i) t_i + v_d^2 t_i\} \quad (13b)$$

where the first sum is over the N_t time steps at time t_i larger than some suitably large initial time, the second sum is over the N_{pt} particles in the ensemble, $v_{l,p}(t_i)$ is the longitudinal velocity of particle p at time t_i, and v_d is the drift velocity along the direction of the field. A similar expression holds for D_t, the other component of the diffusion tensor we have computed, by replacing the displacement and velocity along the field direction x_l and v_l, with the displacement and velocity along the normal direction x_t and v_t, and by replacing the drift velocity v_d with the (vanishing) velocity along the direction normal to the field. Typically, we used ensembles of 16–32 particles. Very long times must be simulated in order to reach the linear time dependence of the mean-square displacement in (13a): times as long as 10 ns for high-mobility compounds, such as III–V's, at low fields and 77 K are required. This accounts for the large statistical noise seen in Fig. 12. Smoothing cubic spline fits of the data are indicated by lines and should be considered no more than a guide for the eye. The energy and momentum relaxation times have been obtained directly from the collision integral

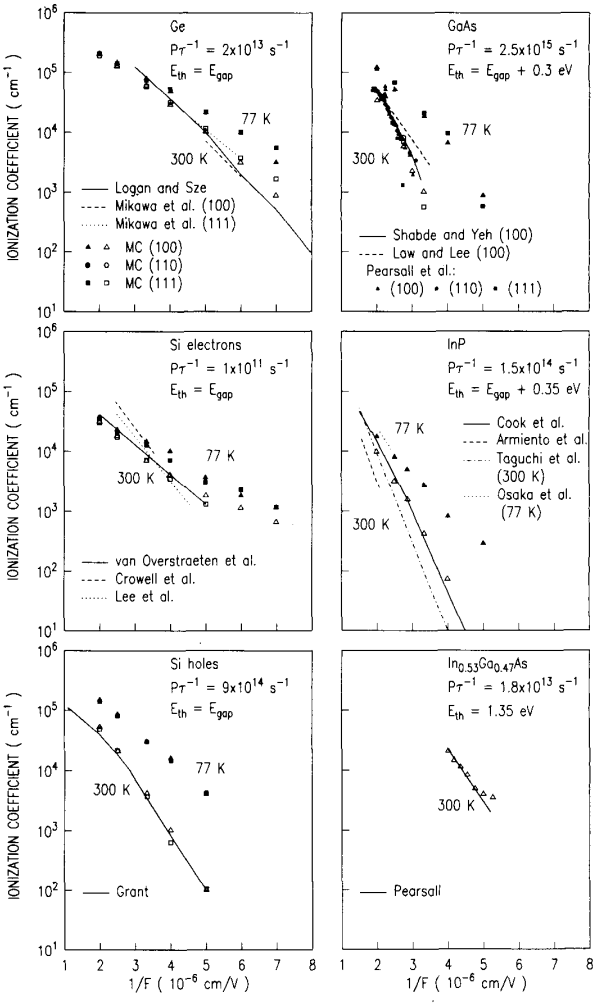

Fig. 10. Impact ionization coefficient α as a function of electric field at 77 and 300 K for a variety of semiconductors obtained from our simulations. Selected experimental data from the literature and the ionization parameters for holes in Si and electrons in $In_{0.53}Ga_{0.47}As$ (not listed in Table IV) are also indicated.

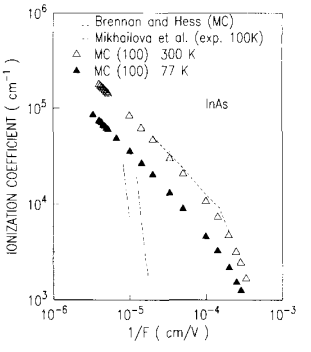

Fig. 11. Impact ionization coefficient α as a function of electric field at 77 and 300 K in InAs compared to the MC results by Brennan and Hess [20] at 77 K (dashed line) and 300 K (dotted line). Note the logarithmic scale for the inverse electric field $1/F$. The range of the experimental data by Mikhailova and colleagues [87], delimited by the two solid lines, is also shown, despite their inconsistency with many other experimental observations, as described in the text.

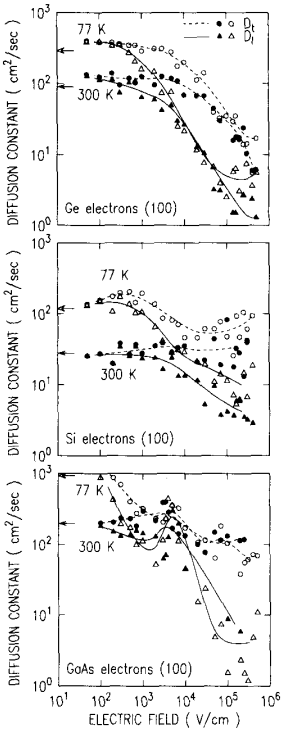

Fig. 12. Longitudinal and transverse electron diffusion constants (D_l and D_t, respectively) in Ge, Si, and GaAs as a function of the electric field in the (100) direction at 77 K (open symbols) and 300 K (solid symbols). The lines are smoothing spline fits shown as a guide for the eye among the noisy simulation results. The arrows (open: 77 K, solid: 300 K) indicate the values obtained from the Einstein relation using the simulation result for the ohmic mobility extracted from Fig. 5.

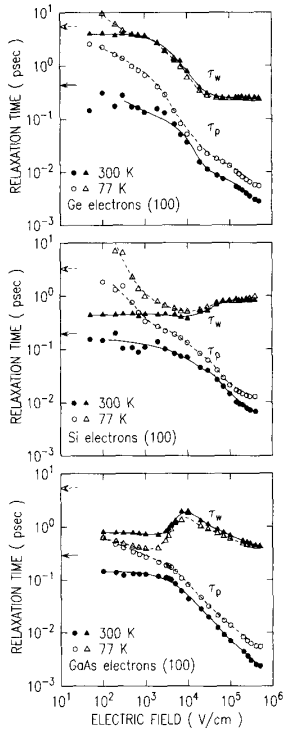

Fig. 13. Energy (triangles) and momentum (circles) relaxation times in Ge, Si, and GaAs as a function of the electric field in the (100) direction at 77 K (open symbols) and 300 K (solid symbols). The lines are smoothing spline fits shown as a guide for the eye. The arrows (open: 77 K; solid: 300 K) indicate the values expected for the momentum relaxation time as obtained from the values of the simulated ohmic mobility and effective masses at the conduction-band bottom.

appearing in the Boltzmann transport equation

$$\frac{1}{\tau_p} \equiv -\frac{\int d\mathbf{k}\, k_l \left(\dfrac{\partial f(\mathbf{k}, t)}{\partial t}\right)_{\text{coll}}}{\int d\mathbf{k}\, k_l f(\mathbf{k}, t)} \tag{14a}$$

where k_l is the longitudinal component of the particle wave vector and

$$\left(\frac{\partial f(\mathbf{k}, t)}{\partial t}\right)_{\text{coll}} = \int d\mathbf{k}'\, W(\mathbf{k}', \mathbf{k}) f(\mathbf{k}') - \int d\mathbf{k}'\, W(\mathbf{k}, \mathbf{k}') f(\mathbf{k}) \tag{14b}$$

where $W(\mathbf{k}, \mathbf{k}')$ is the scattering probability from $\mathbf{k}$ to $\mathbf{k}'$. Using the definition for the total scattering rate

$$\frac{1}{\tau(\mathbf{k})} \equiv \int d\mathbf{k}'\, W(\mathbf{k}, \mathbf{k}') \tag{15}$$

one can see that the MC equivalent of (14a) is given by

$$\frac{1}{\tau_p} = \left[\sum_{\text{collision}} \frac{k_l^{(in)} - k_l^{(fin)}}{\tau(\mathbf{k}^{(in)})}\right] \Big/ \sum_{\text{collision}} k_l^{(in)}. \tag{16a}$$

Similarly, for the energy relaxation rate we have

$$\frac{1}{\tau_w} = \left[\sum_{\text{collision}} \frac{E^{(in)} - E^{(fin)}}{\tau(\mathbf{k}^{(in)})}\right] \Big/ \sum_{\text{collision}} E^{(in)}. \tag{16b}$$

In (16a) and (16a), (*in*) and (*fin*) indicate the values taken immediately before and after every collision.

The diffusion constants shown in Fig. 12 are in good agreement with the experimental data available for Ge and Si, reported in [6] and [7]. For GaAs, the only experimental data at 300 K we are aware of [48], which cover the critical-field region, show an ohmic behavior well represented by our simulations, but a much higher peak value ($\simeq 950$ cm^2/s) at the onset of the Γ-to-L transfer. Similarly, higher values are observed at higher fields. Our MC results are roughly consistent with the results of Fawcett and Rees [89], but we could not reproduce the good agreement between experiments and MC results reported by Pozela and Reklaitis [90], despite our "correct" Γ-L-X ordering and the lower Γ-L intervalley deformation potential we employ. Recently, Mickevicius and Reklaitis [91] have reviewed this problem, discussing additional experimental and theoretical results.

V. Conclusions

We have shown that realistic MC simulations can account for the available experimental information regarding the dependence of carrier drift velocity, impact-ionization coefficients, and diffusivity in (homogeneous) electric field at steady state. The carrier-phonon coupling constants we employ are consistent with recent theoretical estimates and are significantly lower than those used in previous MC simulations. We attribute part

of the difference to the more realistic band structure we have employed, particularly for the satellite valleys (L and X) of some III–V materials. Unfortunately, even for very well studied semiconductors, significant uncertainties are still present in the experimental data. Significant examples are the Γ–L energy splitting in InP, the peak velocity, and field of GaAs at room temperature, impact ionization data in InAs, velocity–field characteristics, and even the band structure of GaP, and the entire velocity–field characteristics of bulk III–V alloys. Device simulations of these semiconductors have to be regarded cautiously. The basic physics is clearly understood, but many quantitative details remain to be settled.

ACKNOWLEDGMENT

The author wishes to thank T. Masselink and N. Braslau for having kindly provided their data prior to publication, J. A. Kash for having pointed out the results of [34] and for discussions about the Γ–L intervalley transition rate in GaAs, S. Tiwari for discussions and help with the critical selection of the bibliography, and S. E. Laux for many discussions. The manuscript has been critically read by D. Arnold, N. Braslau, D. J. DiMaria, S. E. Laux, W. Lee, F. Stern, S. Tiwari, and T. N. Theis.

REFERENCES

[1] M. V. Fischetti and S. E. Laux, "Monte Carlo simulation of transport in technologically significant semiconductors of the diamond and zinc-blende structures. Part II: Submicrometer MOSFET's," this issue, pp. 650–660.

[2] ——, "Monte Carlo analysis of electron transport in small semiconductor devices including band-structure and space-charge effects," *Phys. Rev. B*, vol. 38, pp. 9721–9745, 1988.

[3] M. L. Cohen and T. K. Bergstresser, "Band structures and pseudopotential form factors for fourteen semiconductors of the diamond and zinc-blende structures," *Phys. Rev.*, vol. 141, pp. 789–796, 1966.

[4] C. Canali, C. Jacoboni, F. Nava, G. Ottaviani, and A. Alberigi-Quaranta, "Electron drift velocity in silicon," *Phys. Rev. B*, vol. 12, pp. 2265–2284, 1975.

[5] G. Ottaviani, L. Reggiani, C. Canali, F. Nava, and A. Alberigi-Quaranta, "Hole drift velocity in silicon," *Phys. Rev. B*, vol. 12, pp. 3318–3329, 1975.

[6] R. Brunetti, C. Jacoboni, F. Nava, and L. Reggiani, "Diffusion coefficient of electrons in silicon," *J. Appl. Phys.*, vol. 52, pp. 6713–6722, 1981.

[7] C. Jacoboni, F. Nava, C. Canali, and G. Ottaviani, "Electron drift velocity and diffusivity in germanium," *Phys. Rev. B*, vol. 24, pp. 1014–1026, 1981.

[8] J. Jacoboni, R. Minder, and G. Majni, "Effects of band nonparabolicity on electron drift velocity in silicon above room temperature," *J. Phys. Chem. Solids*, vol. 36, pp. 1129–1133, 1975.

[9] C. Jacoboni and L. Reggiani, "The Monte Carlo method for the solution of charge transport in semiconductors with application to covalent materials," *Rev. Mod. Phys.*, vol. 55, pp. 645–705, 1983.

[10] W. Fawcett, A. D. Boardman, and S. Swain, "Monte Carlo determination of electron transport properties in gallium arsenide," *J. Phys. Chem. Solids*, vol. 31, pp. 1963–1990, 1970.

[11] M. A. Littlejohn, J. R. Hauser, and T. H. Glisson, "Velocity-field characteristics of GaAs with Γ_6^c–L_6^c–X_6^c conduction band ordering," *J. Appl. Phys.*, vol. 48, pp. 4587–4590, 1977.

[12] W. Fawcett and D. C. Herbert, "High-field transport in gallium arsenide and indium phosphide," *J. Phys. C: Solid State Phys.*, vol. 7, pp. 1641–1654, 1974.

[13] D. C. Herbert, W. Fawcett, and C. Hilsum, "High-field transport in indium phosphide," *J. Phys. C: Solid State Phys.*, vol. 9, pp. 3969–3975, 1976.

[14] J. R. Hauser, M. A. Littlejohn, and T. H. Glisson, "Velocity-field relationship of InAs-InP alloys including the effect of alloy scattering," *Appl. Phys. Lett.*, vol. 28, pp. 458–461, 1976.

[15] P. J. Price, "Monte Carlo calculations of electron transport in solids," *Semicond. and Semimetals*, vol. 14, pp. 249–308, 1979.

[16] H. Shichijo and K. Hess, "Band-structure-dependent transport and impact ionization in GaAs," *Phys. Rev. B*, vol. 23, pp. 4197–4207, 1981.

[17] J. Y. Tang and K. Hess, "Impact ionization of electrons in silicon," *J. Appl. Phys.*, vol. 54, pp. 5139–5144, 1983.

[18] J. Y. Tang and K. Hess, "Theory of hot electron emission from silicon into silicon dioxide," *J. Appl. Phys.*, vol. 54, pp. 5145–5151, 1983.

[19] K. Brennan, K. Hess, J. Y. Tang, and G. J. Iafrate, "Transient electronic transport in InP under the conditions of high-field electron injection," *IEEE Trans. Electron Devices*, vol. ED-30, pp. 1750–1754, 1983.

[20] K. Brennan and K. Hess, "High-field transport in GaAs, InP, and InAs," *Solid-State Electron.*, vol. 27, pp. 347–357, 1984.

[21] J. R. Chelikowsky and M. L. Cohen, "Nonlocal pseudopotential calculations for the electronic structure of eleven diamond and zinc-blende semiconductors," *Phys. Rev. B*, vol. 14, pp. 556–582, 1976.

[22] Landolt-Börnstein, *Numerical Data and Functional Relationships in Science and Technology* (New Series), K.-H. Hellwege, Editor in Chief, Group III: *Crystal and Solid State Physics*, vol. 17: *Semiconductors*, O. Madelung, M. Schultz, and H. Weiss, Eds., subvol. a: "Physics of Group IV Elements and III-V Compounds," O. Madelung, Ed. Berlin, Springer-Verlag, 1982.

[23] G. Gilat and L. J. Raubenheimer, "Accurate method for calculating frequency-distribution functions in solids," *Phys. Rev.*, vol. 144, pp. 390–395, 1966.

[24] N. Sano, M. Tomizawa, and A. Yoshii, "Soft and hard ionization thresholds in Si and GaAs," *Appl. Phys. Lett.*, vol. 55, pp. 1418–1420, 1989.

[25] N. Sano, M. Tomizawa, and A. Yoshii, "Monte Carlo analysis of ionization thresholds in Si," *Appl. Phys. Lett.*, vol. 56, pp. 653–655, 1990.

[26] N. Sano, T. Aoki, M. Tomizawa, and A. Yoshii, "Electron transport and impact ionization in Si," *Phys. Rev. B*, vol. 41, pp. 12122–12128, 1990.

[27] J. W. Harrison and J. R. Hauser, "Theoretical calculations of electron mobility in ternary III–V compounds," *J. Appl. Phys.*, vol. 47, pp. 292–300, 1976.

[28] J. Singh and K. K. Bajaj, "A model for high-field transport in alloys: Application to $In_{0.53}Ga_{0.47}As$," *J. Appl. Phys.*, vol. 57, pp. 322–324, 1985.

[29] A. Al-Omar and J. P. Krusius, "Self-consistent Monte Carlo study of high-field carrier transport in heterostructures," *J. Appl. Phys.*, vol. 62, pp. 3825–3835, 1987.

[30] A. Al-Omar, "Hot-electron transport in nanometer scaled graded ternary III–V semiconductor devices," Ph.D. dissertation Cornell University, Ithaca, NY, Aug. 1988.

[31] K. Sadra, C. M. Maziar, B. G. Streetman, and D. S. Tang, "Effects of multiband electron-hole scattering and hole wave-function symmetry on minority-electron transport in GaAs," *J. Appl. Phys.*, vol. 66, pp. 4791–4800, 1989.

[32] J. H. Marsh, "Effect of compositional clustering on electron transport in $In_{0.53}Ga_{0.47}As$," *Appl. Phys. Lett.*, vol. 41, pp. 732–734, 1982.

[33] J. S. Blakemore, "Semiconductor and other major properties of gallium arsenide," *J. Appl. Phys.*, vol. 53, pp. R123–R181, 1982.

[34] M. A. Alekseev, I. Ya. Karlik, D. N. Mirlin, V. F. Sapega, and A. A. Sirenko, "Intra and intervalley electron scattering in the conduction band edge of InP valence band warping," in *Proc. 19th Int. Conf. on the Physics of Semiconductors*, W. Zawadzki, Ed. (Wrocław, Poland, Institute of Physics). Warsaw, Poland: Polish Academy of Sciences, 1988, pp. 1423–1426.

[35] T. Wang and K. Hess, "Calculation of the electron velocity distribution in high electron mobility transistors using an ensemble Monte Carlo method," *J. Appl. Phys.*, vol. 57, pp. 5336–5344, 1985.

[36] S. Adachi, "GaAs, AlAs, and $Al_xGa_{1-x}As$: Materials parameters for use in research and device applications," *J. Appl. Phys.*, vol. 58, pp. R1–R29, 1985.

[37] W. Fawcett, C. Hilsum, and H. D. Rees, "Effects of non-parabolicity of non-ohmic transport in InAs," *Solid State Commun.*, vol. 7, pp. 1257–1259, 1969.

[38] M. Heiblum, M. V. Fischetti, W. P. Dumke, D. J. Frank, I. M. Anderson, C. M. Knoedler, and L. Osterling, "Electron interference effects in quantum wells: Observation of bound and resonant states," *Phys. Rev. Lett.*, vol. 58, pp. 816–819, 1987.
[39] M. Heiblum and M. V. Fischetti, "Ballistic electron transport in hot electron transistors," in *The Physics of Quantum Devices*, F. Capasso, Ed. New Dehli, India: McMillan of India Ltd, 1990, pp. 271–320.
[40] J. Shah, B. Deveaud, T. C. Damen, W. T. Tsang, A. C. Gossard, and P. Lugli, "Determination of the intervalley scattering rates in GaAs by subpicosecond luminescence spectroscopy," *Phys. Rev. Lett.*, vol. 59, pp. 2222–2225, 1987.
[41] O. J. Glembocki and F. H. Pollack, "Calculation of the Γ-Δ electron-phonon and hole-phonon scattering matrix elements in silicon," *Phys. Rev. Lett.*, vol. 48, pp. 413–416, 1982.
[42] S. Zollner, S. Gopalan, and M. Cardona, "Intervalley deformation potentials and scattering rates in zinc blende semiconductors," *Appl. Phys. Lett.*, vol. 54, pp. 614–616, 1989.
[43] B. S. Wang, Z. Q. Gu, J. Q. Wang, and M. F. Li, "Ab Initio pseudopotential calculations of optical-phonon deformation potentials in zinc-blende semiconductors," *Phys. Rev. B*, vol. 39, pp. 12789–12793, 1989.
[44] S. N. Grinyaev, G. F. Karavaev, and V. G. Tyuterev, "Calculation of the parameters of intervalley scattering by phonons in III–V semiconductor crystals," *Sov. Phys.—Semicond.*, vol. 23, pp. 905–907, 1989.
[45] J. Shah, "Photoexcited hot carriers: From cw to fs in 20 years," *Solid-State Electron.*, vol. 32, pp. 1051–1056, 1989.
[46] J. A. Kash, R. G. Ulbrich, and J. C. Tsang, "Quantitative measurements of intervalley and carrier-carrier scattering in GaAs with hot (e, $A^{(1)}$) luminescence," *Solid-State Electron.*, vol. 32, pp. 1277–1281, 1989.
[47] W. T. Masselink, N. Braslau, W. I. Wang, and S. L. Wright, "Electron velocity and negative differential mobility in AlGaAs/GaAs modulation-doped heterostructures," *Appl. Phys. Lett.*, vol. 51, pp. 1533–1535, 1987.
[48] J. G. Ruch and G. S. Kino, "Transport properties of GaAs," *Phys. Rev.*, vol. 174, pp. 921–931, 1968.
[49] T. H. Windhorn, T. J. Roth, L. M. Zinkiewicz, O. L. Gaddy, and G. E. Stillman, "High field temperature dependent electron drift velocities in GaAs," *Appl. Phys. Lett.*, vol. 40, pp. 513–515, 1983.
[50] P. A. Houston and A. G. R. Evans, "Electron drift velocity in n-GaAs at high electric fields," *Solid-State Electron.*, vol. 20, pp. 197–204, 1977.
[51] P. Smith, M. Inoue, and J. Frey, "Electron velocity in Si and GaAs at very high electric fields," *Appl. Phys. Lett.*, vol. 37, pp. 797–798, 1980.
[52] T. H. Windhorn, L. W. Cook, M. A. Haase, and G. E. Stillman, "Electron transport in InP at high electric fields," *Appl. Phys. Lett.*, vol. 42, pp. 725–727, 1983.
[53] P. M. Boers, "Measurements on dipole domains in indium phosphide," *Phys. Lett.*, vol. 34A, pp. 329–330, 1971.
[54] P. N. Robson, K. E. Potter, and A. Majerfeld, "Capacitive probe measurements of dipole domains in InP," *IEEE Trans. Electron Devices*, vol. ED-22, pp. 569–575, 1975.
[55] A. Majerfeld, K. E. Potter, and P. N. Robson, "Subthreshold velocity-field characteristics for bulk and epitaxial InP," *J. Appl. Phys.*, vol. 45, pp. 3681–3682, 1974.
[56] K. Brennan, D. H. Park, K. Hess, and M. A. Littlejohn, "Theory of velocity-field relation in AlGaAs," *J. Appl. Phys.*, vol. 63, pp. 5004–5008, 1988.
[57] D. Matz, "Effect of nonparabolicity on non-ohmic transport in InSb and InAs," *Phys. Rev.*, vol. 168, pp. 843–849, 1968.
[58] F. Kuchar, G. Bauer, and H. Hillbrand, "NDC instability in n-InAs in a transverse magnetic field," *Phys. Status Solidi (a)*, vol. 17, pp. 491–496, 1973.
[59] Z. Dobrovol'skis, K. Grigoras, and A. Krotkus, "Measurements of the hot-electron conductivity in semiconductors using ultrafast electric pulses," *Appl. Phys. A*, vol. 48, pp. 245–249, 1989.
[60] A. Plitnikas, A. Krotkus, and Z. Dobrovol'skis, "Current-voltage characteristics of compensated indium arsenide in strong electric fields," *Sov. Phys.—Semicond.*, vol. 16, pp. 622–625, 1982.
[61] W. P. Dumke, "Theory of avalanche breakdown in InSb and InAs," *Phys. Rev.*, vol. 167, pp. 783–789, 1968.
[62] T. H. Windhorn, L. W. Cook, and G. E. Stillman, "The electron velocity-field characteristics for n-$In_{0.53}Ga_{0.47}As$ at 300 K," *IEEE Electron Devices Lett.*, vol. EDL-3, pp. 18–20, 1982.
[63] T. H. Windhorn, L. W. Cook, and G. E. Stillman, "Temperature dependent electron velocity-field characteristics for $In_{0.53}Ga_{0.47}As$ at high electric fields," *J. Electron. Mat.*, vol. 11, pp. 1065–1082, 1982.
[64] E. Kobayashi, C. Hamaguchi, T. Matsuoka, and K. Taniguchi, "Monte Carlo study of hot electron transport in an InGaAs/InAlAs single heterostructure," *IEEE Trans. Electron Devices*, vol. 36, pp. 2353–2360, 1989.
[65] S. Krishnamurthy and A. Sher, "Velocity-field characteristics of III–V semiconductor alloys: Band-structure influences," *J. Appl. Phys.*, vol. 61, pp. 1475–1479, 1987.
[66] K. Y. Cheng, A. Y. Chao, S. B. Christman, T. P. Pearsall, and J. E. Rowe, "Measurement of the Γ-L separation in $Ga_{0.47}In_{0.53}As$ by ultraviolet photoemission," *Appl. Phys. Lett.*, vol. 40, pp. 423–425, 1982.
[67] R. H. Johnson and O. Eknoyan, "High-field electron drift velocity measurements in gallium phosphide," *J. Appl. Phys.*, vol. 58, pp. 1402–1403, 1985.
[68] V. Arora, D. S. L. Mui, and H. Morkoç, "High-field electron drift velocity and temperature in gallium phosphide," *J. Appl. Phys.*, vol. 61, pp. 4703–4704, 1987.
[69] E. O. Kane, "Electron scattering by pair production in silicon," *Phys. Rev.*, vol. 159, pp. 624–631, 1967.
[70] F. Capasso, "Physics of avalanche photodiodes," *Semicond. Semimetals*, vol. 22, pp. 1–172, 1985.
[71] R. A. Logan and S. M. Sze, "Avalanche multiplication in Ge and GaAs p-n junctions," *J. Phys. Soc. Japan., Suppl.*, vol. 21, p. 434, 1966.
[72] T. Mikawa, S. Kagawa, T. Kaneda, Y. Toyama, and O. Mikami, "Crystal orientation dependence of ionization rates in germanium," *Appl. Phys. Lett.*, vol. 37, pp. 387–389, 1980.
[73] R. van Overstraeten and H. DeMan, "Measurement of the ionization rates in diffused silicon p-n junctions," *Solid-State Electron.*, vol. 13, pp. 583–608, 1970.
[74] C. R. Crowell and S. M. Sze, "Temperature dependence of avalanche multiplication in semiconductors," *Appl. Phys. Lett.*, vol. 9, pp. 242–244, 1966.
[75] C. A. Lee, R. A. Logan, R. L. Batdorf, J. J. Keimack, and W. Wiegmann, "Ionization rates of holes and electrons in silicon," *Phys. Rev.*, vol. 134, pp. A761–A773, 1964.
[76] W. N. Grant, "Electron and hole ionization rates in epitaxial silicon at high electric fields," *Solid-State Electron.*, vol. 16, pp. 1189–1203, 1973.
[77] S. N. Shadbe and C. Yeh, "Ionization rates in $(Al_xGa_{1-x})As$," *J. Appl. Phys.*, vol. 41, pp. 4743–4744, 1970.
[78] H. D. Law and C. A. Lee, "Interband scattering effects on secondary ionization coefficients in GaAs," *Solid-State Electron.*, vol. 21, pp. 331–340, 1978.
[79] T. P. Pearsall, F. Capasso, R. E. Nahory, M. A. Pollack, and J. R. Chelikowsky, "The band structure dependence of impact ionization by hot carriers in semiconductors," *Solid-State Electron.*, vol. 21, pp. 297–302, 1978.
[80] C. A. Armiento, S. H. Groves, and C. E. Hurwitz, "Ionization coefficients of electrons and holes in InP; photomultiplication measurements," *Appl. Phys. Lett.*, vol. 35, pp. 333–335, 1979.
[81] L. W. Cook, G. E. Bulman, and G. E. Stillman, "Electron and hole impact ionization coefficients in InP determined by photomultiplication measurements," *Appl. Phys. Lett.*, vol. 40, pp. 589–591, 1982.
[82] K. Taguchi, T. Toshitaka, Y. Sugimoto, K. Makita, and H. Ishihara, "Temperature dependence of impact ionization coefficients in InP," *J. Appl. Phys.*, vol. 59, pp. 476–481, 1986.
[83] N. Tabatabaie, V. M. Robbins, N. Pan, and G. E. Stillman, "Impact ionization coefficients in (111) InP," *Appl. Phys. Lett.*, vol. 46, pp. 182–184, 1985.
[84] F. Osaka, Y. Kishi, M. Kobayashi, and T. Mikawa, "Low-temperature impact ionization rates in (111) oriented InP," *Appl. Phys. Lett.*, vol. 47, pp. 865–866, 1985.
[85] T. P. Pearsall, "Impact ionization rates for electrons and holes

in $Ga_{0.47}In_{0.53}As$," *Appl. Phys. Lett.*, vol. 36, pp. 218–220, 1980.
[86] G. Bauer and F. Kuchar, "Impact ionization in heavily doped n-InAs and n-InSb," *Phys. Status Solidi (a)*, vol. 13, pp. 169–177, 1972.
[87] M. P. Mikhailova, D. N. Nasledov, and S. V. Slobodchikov, "Avalanche multiplication in and ionization coefficient of p-n junctions in InAs," *Sov. Phys.—Semicond.*, vol. 1, pp. 94–97, 1967.
[88] C. L. Anderson and C. R. Crowell, "Threshold energies for electron-hole production by impact ionization in semiconductors," *Phys. Rev. B*, vol. 5, pp. 2267–2272, 1972.
[89] W. Fawcett and H. D. Rees, *Phys. Lett.*, vol. 11, p. 731, 1969.
[90] J. Pozela and A. Reklaitis, "Diffusion coefficient of hot electrons in GaAs," *Solid State Commun.*, vol. 27, pp. 1073–1077, 1978.
[91] R. Mickevicius and A. Reklaitis, "Electron intervalley scattering in gallium arsenide," *Semicond. Sci. Technol.*, vol. 5, pp. 805–812, 1990.

*

Massimo V. Fischetti was born in Italy. He received the Ph.D. degree in theoretical physics from the University of California, Santa Barbara.

He joined the IBM T. J. Watson Research Center, Yorktown Heights, NY, in 1983. His primary interests concern the high-field properties of silicon dioxide and semiconductors.